

Mechanism for acetate formation in CO₍₂₎ reduction on Cu: Selectivity trends with pH and nanostructuring derive from mass transport

Hendrik H. Heenen,[†] Georg Kastlunger,[†] Haeun Shin,[‡] Sean Overa,[‡] Joseph A. Gauthier,[¶] Feng Jiao,^{*,‡} and Karen Chan^{*,†}

[†]*Department of Physics, Technical University of Denmark, DK-2800, Kgs. Lyngby, Denmark*

[‡]*Center for Catalytic Science and Technology, Department of Chemical and Biomolecular Engineering, University of Delaware, Newark, DE, USA*

[¶]*SUNCAT Center for Interface Science and Catalysis, Department of Chemical Engineering, Stanford University, Stanford, California 94305, United States*

[§]*SUNCAT Center for Interface Science and Catalysis, SLAC National Accelerator Laboratory, 2575 Sand Hill Road, Menlo Park, California 94025, United States*

E-mail: jjiao@udel.edu; kchan@fysik.dtu.dk

Abstract

Nanostructured Cu catalysts have increased the selectivities and geometric activities for high value C-C coupled (C₂) products in the electrochemical CO₍₂₎ reduction reaction (CO₍₂₎RR). The selectivity among the high-value C₂ products is also altered, where for instance the yield of acetate increases with alkalinity and is dependent on the catalyst morphology. The reaction mechanisms behind the selectivity towards acetate vs. other C₂ products remain controversial. In this work, we elucidate the reaction

mechanism behind selectivity towards acetate by using *ab-initio* simulations, a coupled kinetic-transport model, and loading experiments. We find that trends in acetate selectivity can be rationalized from variations in electrolyte pH and the local mass transport properties of the catalyst and not from changes of Cu’s intrinsic activity. The selectivity mechanism originates in the transport of ketene, a stable (closed shell) intermediate, away from the catalyst surface into solution where it reacts to acetate. While such a mechanism has not yet been discussed in CO₍₂₎RR, variants of it may explain similar selectivity fluctuations observed for other stable intermediates like CO and acetaldehyde. Our proposed mechanism suggests acetate selectivity to increase with increasing pH, decreasing catalyst roughness and to significantly vary with applied potential.

Broader context

The electrochemical reduction of CO₂ enables the storage of renewable energy in carbon neutral fuels while simultaneously reducing greenhouse gas emissions. Recent developments have led to an almost commercially viable process exploiting nanostructured Cu catalysts and gas-diffusion electrodes, which produce high value C₂ products at high current densities. The selectivity between these C₂ products, which mainly consist of ethylene, ethanol and acetate, still poses a challenge to maximize cost efficiency. In this joint experimental-theoretical work, we elucidate the selectivity mechanism towards acetate vs. ethylene and ethanol using a multi-scale modelling approach with near quantitative agreement to experiment. We determine that transport properties at the catalyst surface are pivotal in steering selectivity between acetate and other C₂ products. While our insights deduce design rules for an acetate rich or poor CO₂ reduction process, they can be generalized to understand selectivity changes with catalyst roughness of other products and processes.

Introduction

The electrochemical reduction of CO (CORR) and CO₂ (CO₂RR) has the potential to enable the storage of renewable energy via the production of carbon neutral fuels. CO₍₂₎RR Cu electrocatalysts have thereby been extensively explored, since Cu is the only material able to produce high value C-C coupled products (C₂).¹ Improvements in activity and selectivity of these catalysts are urgently needed to enable the commercialization and cost-effective operation of CO₍₂₎RR electrolyzers.^{2,3} To this end, two key developments have been introduced over the last decade. Firstly, gas diffusion electrodes (GDE) in combination with flow cell setups achieve significantly higher current densities over traditional H-cell setups, which suffer from mass transport limitations.⁴⁻⁶ Secondly, various means of nanostructuring Cu have been explored in order to increase the active surface area and to tune the selectivity towards high value products.^{1,7-10} For instance, nanostructured catalysts in a GDE/flow-cell setup have led to significantly increased selectivities towards acetate under alkaline conditions.^{11,12} Originally considered a minor product, under these specific conditions, acetate has Faradaic efficiencies comparable to ethylene and ethanol, the two major C₂ products produced by Cu under less alkaline conditions. To date, there is no consensus on how nanostructuring or mass transport impacts the intrinsic activity and selectivity of Cu towards the possible C₂ products.^{9,10}

In this paper, we suggest that nanostructuring of Cu changes the selectivity for acetate vs. other C₂ products through altering the mass transport of products away from the electrode, and not through changes in intrinsic activity via new active sites.¹² We suggest that acetate forms via a solution reaction of ketene with OH⁻, which is heavily affected by transport and electrolyte pH. We derive our insight from a comprehensive examination of reported experimental activities of Cu catalysts normalized to active surface area, an *ab-initio* derived microkinetic model coupled to mass transport, and through activity measurements on Cu nanoparticles at a range of loadings.

Previous computational studies have attempted to rationalize the acetate activity and

selectivity through reaction thermodynamics and barriers.^{11–13} However, the dependence of acetate selectivity on pH and potential remained an open question, and differences in various Cu samples were assumed to arise from different active sites. We suggest that such mechanisms are inconsistent with ECSA-normalized activity of all reported Cu catalysts and the potential dependence of observed selectivity. In contrast, our computational model shows that the interplay of kinetics and mass transport determines the acetate selectivity vs. other C₂ products. The model agrees with the experimentally observed trends in the dependence of acetate selectivity on potential, electrolyte pH, and catalyst roughness. Previously, transport limitations have already been suggested to alter selectivity behavior between CO₍₂₎RR products and H₂ by affecting reactant concentrations and local pH at the catalyst surface.^{6,14–17} This work showcases how mass transport also controls the competition between the desorption and the further reduction of stable intermediates with a corresponding impact on selectivity. Such a concept has been similarly proposed for stable intermediates in ORR and methanol oxidation.¹⁸ This principle is, therefore, generalizable to controlling the selectivity of other stable intermediates in CO₍₂₎RR like CO and acetaldehyde. Overall, our combined analysis of experiments and simulations suggests the following insights relevant for the design of CO₍₂₎RR electrolyzers: acetate selectivity vs. other C₂ products is optimized by a high interfacial and bulk pH and a low, microscopic surface roughness of the Cu catalyst.

Results & Discussion

ECSA normalized current densities suggest no change in intrinsic activity to C₂ products with nanostructuring

Firstly, we emphasize that the only rigorous metric of intrinsic activity in catalysis is the turnover frequency (TOF),¹⁹ which is, under fast mass transport conditions, directly related to the reaction energetics via the Arrhenius law. Onset potentials towards various products (which depend on the sensitivity of the characterization technique) may give an approximate

idea of the relative activities to various products, and Faradaic efficiencies are important from an application standpoint. However, neither metric reflects the intrinsic activity nor the associated activation energies. Without an estimate of the active site densities, ECSA-normalized current densities, j_{ECSA} , are the best available estimates for the TOF and intrinsic activity,^{1,10,20} accurate to the extent of the variations in active site densities amongst the catalysts considered.

Fig. 1 shows j_{ECSA} for various Cu catalysts in both GDE and H-cell setups towards the sum of all C₂ products in CO₍₂₎RR and specifically to ethylene, ethanol, and acetate. Even under a wide range of reaction conditions (CO and CO₂ as the reactant, different electrolytes with pH ranging from 6.8 to 14.3, wide potential range) and catalyst morphologies (from Cu single crystals and foils to deliberately roughened oxide-derived (OD) Cu, nanowires and nanoparticles) we find the currents to overlap within an order of magnitude for data sets without obvious transport limitations (blue lines in Fig. 1, which all correspond to GDE setups). Larger deviations are only seen for data collected in traditional H-cell setups where transport limitations are present at lower overpotentials (gray lines in Fig. 1).

Recent reviews have pointed out the similar intrinsic activities amongst different types of Cu catalysts towards all CO₍₂₎RR products.^{1,10} We confirm this observation in Fig. 1, and in addition we highlight the similar activity of different Cu catalysts for the individual major C₂ products. These partial current densities change only within an order of magnitude which suggests a uniform intrinsic activity towards the different products and therefore the same active site on the different catalysts. If the order-of-magnitude change in partial current densities were to arise instead from a change in active site, the difference in the activation energies towards a given product would be around $\leq 0.05\text{-}0.10$ eV, assuming similar active site densities (and following the Arrhenius law). The expected electronic effects of changing an active site are, however, usually between 0.3 and 1.0 eV¹⁹ and would result in significantly larger variation of 5 to 15 orders of magnitude in the TOF and corresponding partial current densities. Therefore, we hypothesize that possible changes in selectivity arise only due to

changes in active site densities, electrolyte pH or transport limitations.

Fig. 1 also shows a subtly stronger variation of the acetate currents in comparison to ethylene and ethanol although all C_2 s follow nearly the same potential behavior (or Tafel slope). While the former is a function of the electrolyte pH and catalyst morphology (see below), the latter indicates the same rate determining step for these C_2 products. In what follows, we derive a comprehensive mechanism for acetate which rationalizes the dependence of its activity on pH and catalyst morphology.

***Ab initio* calculations suggest a solution phase reaction of ketene and OH^- towards acetate**

Fig. 2 shows our proposed mechanism of the selectivity determining steps (SDS) towards acetate vs. other major C_2 products, determined on the basis of DFT simulations. Central to this mechanism is the ketene intermediate as also previously suggested,^{8,11,13} but in both its desorbed ($H_2CCO(aq)$) and adsorbed (H_2CCO^*) state. As shown in Fig. 2, a coupled proton-electron transfer (CPET) to $HCCO^*$ leads to the formation of the stable ketene molecule, desorbed from the surface. This reaction step is pivotal since past its formation, $H_2CCO(aq)$ can either react with OH^- to acetate in solution (a well known reaction²⁹) or readsorb and get further reduced to other C_2 products. Either pathway is differently influenced by pH, (ketene) transport, and potential. The elementary reactions making up this branching point evolve around two SDS as indicated in Fig. 2:

1. (SDS-1) The solution reaction vs. re-adsorption of desorbed ketene
2. (SDS-2) The CPET reaction of H_2CCO^* towards other C_2 products vs. the desorption of readsorbed ketene

Firstly, we note that SDS-1 is dependent on the concentration of $H_2CCO(aq)$ and OH^- at the catalyst surface which depends strongly on mass transport. Secondly, we note that SDS-1 involves the competition between two chemical steps while SDS-2 between a chemical and

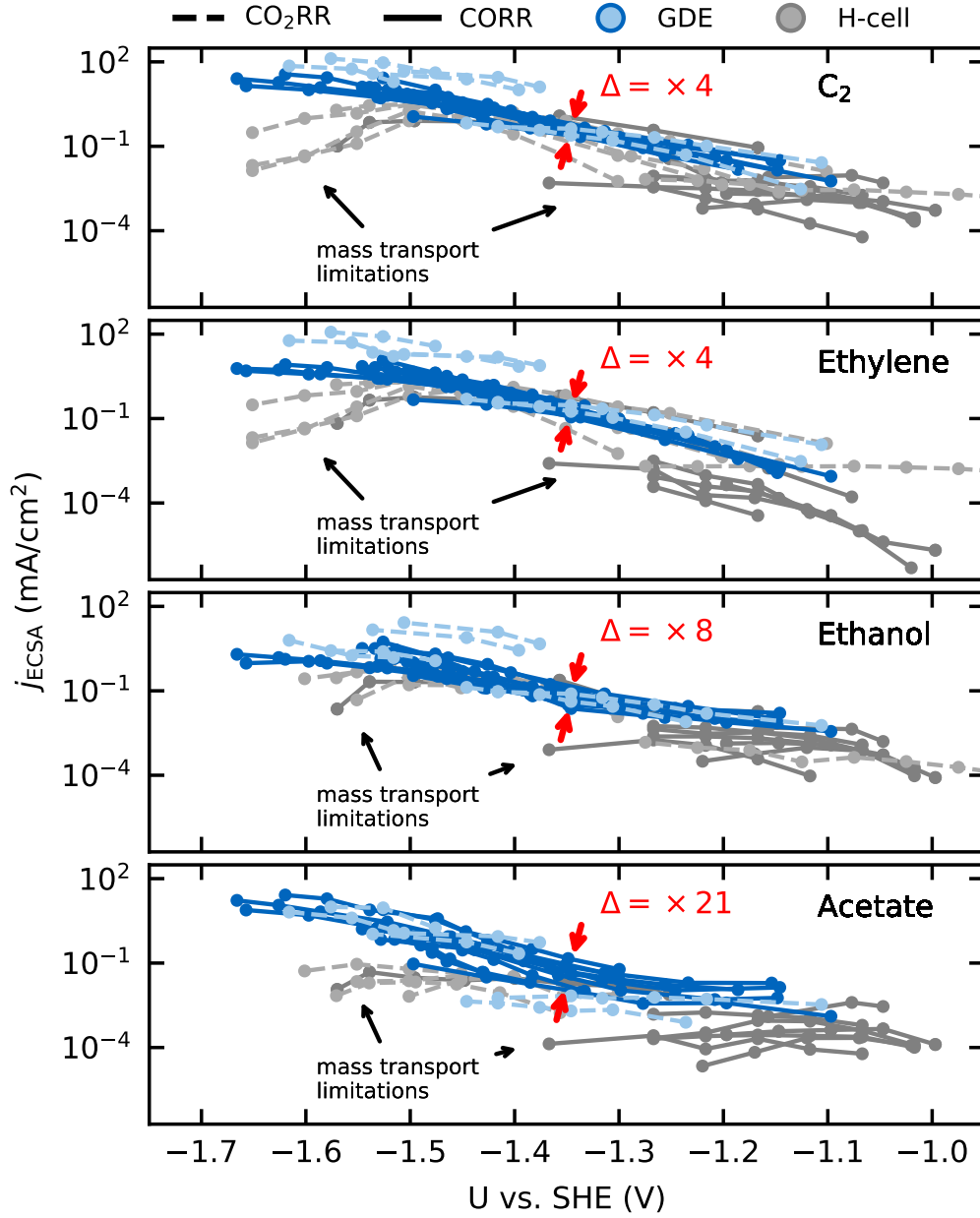


Figure 1: ECSA normalized partial current densities against U_{SHE} for C_2 (top), ethylene (upper center), ethanol (lower center), and acetate (bottom) adapted from different CO_2RR (dashed lines) and CORR (solid lines) studies conducted in a GDE/flow-cell setup (lightblue / blue) or a conventional H-cell setup (lightgray / gray). Each line represents an individual data set of same reaction conditions. The GDE data is adapted from 4, 11, 21–25 and the H-cell data from 7, 8, 26–28. The red arrows indicate the factor in variation of j_{ECSA} (Δ) at $-1.35 U_{\text{SHE}}$.

an electrochemical step. Acetate selectivity of SDS-1 is therefore independent of potential, while SDS-2 is not. The concentration and potential (in)dependence have an important impact on the selectivity, as we detail below.

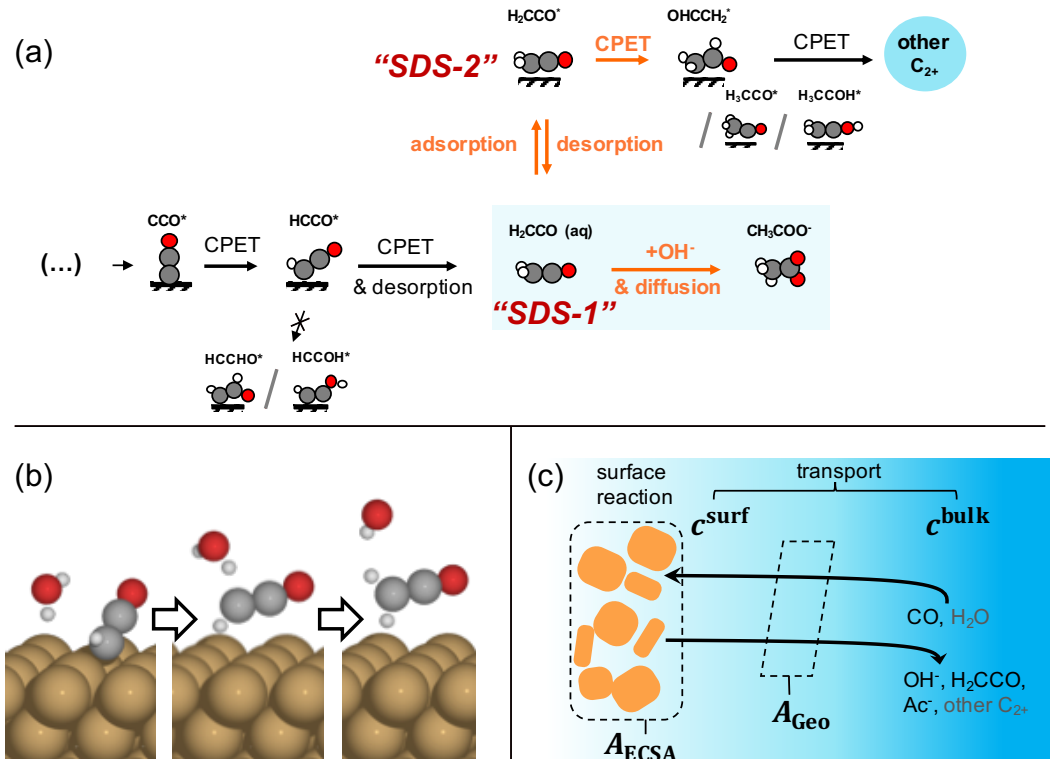


Figure 2: (a) Schematic of the Ketene pathway. We show the mechanism we investigated in our model, i.e. after the RDS and including the two selectivity-determining steps, “SDS-1” and “SDS-2” towards acetate via a solution reaction or the further reduction of the adsorbed ketene (H_2CCO^*) to form other C_2 products. We also depict the excluded alternative reduction steps. (b) Illustration of the simultaneous desorption and reduction of $\text{HCCO}^* \rightarrow \text{H}_2\text{CCO}(\text{aq})$ on Cu(100) as obtained from NEB simulations. (c) Schematic of the mass transport. CO , OH^- , H_2CCO , and Ac^- are considered for transport while H_2O and other C_2 are neglected (grey color). As indicated, the transport scales with geometric area A_{Geo} while processes on the catalyst surface scale with A_{ECSA} .

We derived and validated this mechanism using density functional theory (DFT) calculations. In our derivation, we assume the same rate determining step (RDS) for all C_{2+} products based on previous experimental and theoretical studies, which has been suggested to either be a CO-CO dimerization^{30,31} or the protonation of the OCCO^* intermediate with water as the proton donor.³² The same RDS is consistent with the range of similar Tafel

slopes and the overall similar pH dependence shared among the considered C₂ products (acetate, ethanol, ethylene)¹¹ (see Fig. 1 above). Such a shared and early RDS means that energetics of following intermediates have no effect on the activity towards the sum of all C₂ products, and only affect the selectivity amongst them. We evaluate our suggested reaction mechanism on representative facets: Cu(111) and Cu(100) terraces and Cu(110) and Cu(211) as steps. On all facets considered, the free energies of all steps are mostly downhill and any uphill step is well below 0.75 eV (see Fig. 3) which makes the mechanism feasible at room temperature.¹⁹ We also evaluated the chemical and CPET barriers at a constant potential³³(see methods and Sec. 3 in the SI) around SDS-1 and SDS-2 which are also low enough to lead to measurable rates at room temperature (see Fig. 3, and Fig. S4 and Tab. S1 in the SI). An only exception is an insurmountable re-adsorption barrier for ketene on Cu(111) and Cu(110), which makes these facets inactive for the proposed mechanism to other C₂ products (see Fig. 3 and Sec. 5.5 in the SI). We emphasize that the direct HCCO* → H₂CCO(aq) step was an explicit result from the minimum transition state search and occurs on all investigated facets. The suggested solution reaction of ketene to acetate is consistent with C¹⁸O⁴ and H₂¹⁸O³⁴ isotope labeling experiments. Further, we note that a similar desorption and re-adsorption step has also been suggested for the acetaldehyde intermediate following operando mass spectrometry experiments.^{35,36}

Acetate selectivity is determined by the interplay of kinetics, mass transport, and electrode roughness

To investigate the selectivity behavior we couple a DFT-derived microkinetic model with a mass transport model. The microkinetic model describes the surface reactions of our proposed reaction mechanism to acetate and other C₂ products (see Fig. 2 and SI Sec. 5.1). The mass transport model describes the transport according to the conditions of CORR operation in a GDE/flow cell setup (with corresponding pH, reactants, and diffusion lengths). These parameters are chosen since in this mode of operation acetate is most frequently

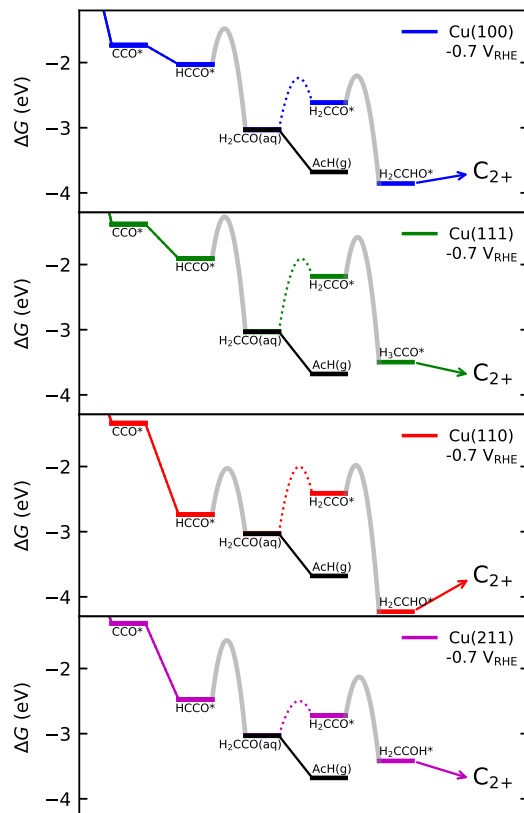


Figure 3: Free energy diagrams for the suggested ketene pathway (see text) on Cu(100), Cu(111), Cu(110), and Cu(211) at -0.7 V vs. RHE (pH=14). Depicted is the considered division into the pathways including reduction of $^*\text{H}_2\text{CCO}$ (colored) and the desorption of ketene and its hydrolysis to acetate (black), respectively. The adsorption barrier of ketene (dotted) and the approximated electrochemical barriers (gray, see methods) are shown.

observed.^{4,8,11,21,26} We only consider the dominant pathway for the acetate formation (i.e. $\text{CO}_{(2)}\text{RR}$ at cathode) in this study, although acetate could also be formed through a partial oxidation of ethanol (the product of $\text{CO}_{(2)}\text{RR}$) at anode in certain cell configurations.²¹

In our microkinetic model we fit the RDS for the C_2 products to the ECSA normalized activity found in experiment (see SI Sec. 5.1). Further, we apply our DFT-derived energies for Cu(100) in the microkinetic model, though the quantitative behavior captured by the model is insensitive to most of the energetics (see SI Sec. 5.5). The only important parameters are the re-adsorption, desorption, and CPET barrier of the ketene intermediate, where we applied a correction of 0.29 eV to the free energy of $\text{H}_2\text{CCO}(\text{aq})$ at the interface (see SI Sec. 5.5.1).

For the description of the mass transport, we use a 1D-mass transport model where we account for the diffusion of CO, OH^- , and H_2CCO as well as the solution reaction of H_2CCO and OH^- to acetate,^{17,37} as illustrated by Fig. 2 and S8. We also include a Sherwood relation to describe the convective mass transport encountered in a flow cell. It describes the diffusion of species from the bulk of the flowing electrolyte to the electrode surface^{38–40} (see methods and SI Sec. 5).

Within our 1D approximation, the effect of the nanostructuring of Cu is captured only by a single roughness factor ρ , and we assume a constant active site density. Note that ρ is a *microscopic* roughness, which reflects the local curvature and porosity of the nanostructured Cu surface. Therefore, in contrast to the ratio of active area and geometric area ($A_{\text{ECSA}}/A_{\text{geo}}$), ρ as we define here does not shift with the loading of a given type of nanostructured Cu. As discussed later, this distinction is important, and arises from the short diffusion length scales in the presence of the rapid solution reaction treated here.

Mass transport limitations give rise to changes in the microscopic reaction environment at the catalyst surface through changes in the surface concentrations (c^{surf}) of individual species (in our case of CO, OH^- , and H_2CCO). Increasing flux and current densities at higher overpotentials give rise to increased concentration gradients, such that the surface

concentrations of reactants ($c_{\text{CO}}^{\text{surf}}$) decrease while those of the products ($c_{\text{OH}^-}^{\text{surf}}$ and $c_{\text{H}_2\text{CCO}}^{\text{surf}}$) increase (see Figs. 4c,d,e).

The simulated geometric current densities ($j_{\text{geo}}^{\text{C}_2}$) are shown in the top panel of Fig. 4a. The maximum $j_{\text{geo}}^{\text{C}_2}$ reached at high overpotentials (more negative U) reflects the CO diffusion limited current density (see Fig. 4c showing the depletion of CO at the surface, $c_{\text{CO}}^{\text{surf}}$). At lower overpotentials, the linear dependence of $j_{\text{geo}}^{\text{C}_2}$ on the catalyst ρ reflects the linear dependence of $j_{\text{geo}}^{\text{C}_2}$ on A_{ECSA} .

The bottom panel in Fig 4a shows the computed selectivity of acetate vs. the total C_2 products ($S_{\text{Ac}^-}^{\text{C}_2}$). In general, $S_{\text{Ac}^-}^{\text{C}_2}$ increases as bulk pH increases and ρ decreases. These trends arise from the competition between the transport of $\text{H}_2\text{CCO}(\text{aq})$ species away from the electrode, and the surface kinetics in SDS-1 (see Fig. 2). The *relative* rate of transport is accelerated with both increasing pH (and correspondingly increased rates of the solution reaction) and decreasing ρ (effectively slower kinetics relative to transport), which leads to a higher acetate selectivity.

The U-shaped selectivity curve vs. potential arises from the following:

- (i) at low overpotentials: The selectivity towards other C_2 products is limited by the CPET to H_2CCO^* (in SDS-2). With decreasing potential this surface reaction becomes more facile while the selective steps towards acetate does not involve any CPET steps. Therefore, as potential decreases the selectivity towards C_2 products increases and that towards acetate decreases.
- (ii) at high overpotentials: The CPET to H_2CCO^* is facile. The selectivity is then determined by $\text{H}_2\text{CCO}(\text{aq})$ readsorption vs. the solution phase reaction of $\text{H}_2\text{CCO}(\text{aq})$ with OH^- (in SDS-1). The build-up of OH^- at increasing overpotentials (local pH, see concentration profile in Fig. 4d) favors the latter reaction and leads to an uptick in acetate selectivity.

The increasing limitations in transport of products away from the surface at increasing

overpotential and corresponding current densities are consistent with the build up in the surface concentrations of the $\text{OH}^-(\text{aq})$ and $\text{H}_2\text{CCO}(\text{aq})$, i.e. of $c_{\text{OH}^-}^{\text{surf}}$ and $c_{\text{H}_2\text{CCO}}^{\text{surf}}$ (Figs. 4f,e). With increasing bulk pH $c_{\text{OH}^-}^{\text{surf}}$ increases and $c_{\text{H}_2\text{CCO}}^{\text{surf}}$ decreases where the latter is due to the accelerated solution phase reaction. The trends in the $c_{\text{H}_2\text{CCO}}^{\text{surf}}$ and $c_{\text{OH}^-}^{\text{surf}}$ with respect to ρ are more nuanced. At low overpotentials, an increased ρ gives a higher production rate of $\text{OH}^-(\text{aq})$ and $\text{H}_2\text{CCO}(\text{aq})$, and consequently *more* build up in both $c_{\text{H}_2\text{CCO}}^{\text{surf}}$ and $c_{\text{OH}^-}^{\text{surf}}$. At high overpotentials, where the production of $\text{OH}^-(\text{aq})$ and $\text{H}_2\text{CCO}(\text{aq})$ is limited by CO transport to the surface, the main impact of increasing ρ is a greater rate of H_2CCO re-adsorption and subsequent production of other C_2 vs. a fixed rate of H_2CCO transport away, which leads to a change in the steady-state re-adsorption equilibrium. This yields an earlier levelling off with negative potential of $c_{\text{H}_2\text{CCO}}^{\text{surf}}$ with increasing ρ .

The complex selectivity behavior of our simulations is consistent with experiments as shown in Fig. 4b. We compare to experimental data from 4, 11 which is based on conditions equivalent to our simulations (CORR in a GDE/flow-cell setup). Different Cu-catalyst morphologies are included in this data with nanosheets (Cu-NS), micron sized particles (Cu- μP), and oxide-derived Cu (OD-Cu). The roughness of these catalysts was determined to be 5, 15, and 65, respectively, via capacitance measurements.^{4,11} Since the catalyst loadings were comparable amongst these samples, the differences in the roughness should arise mostly from microscopic variations amongst the catalysts. We therefore took these roughness values to be the microscopic roughness ρ in our model. In general, we find good agreement for $j_{\text{geo}}^{\text{C}_2}$ between theory and experiment regarding the limiting behavior of CO diffusion and the scaling with respect to ρ . The acetate selectivity $S_{\text{Ac}^-}^{\text{C}_2}$ also shows a very good agreement for the pH, ρ and potential dependence. The trends in roughness and electrolyte pH align between simulations and experiments, i.e. higher acetate selectivity with lower roughness and higher pH. Also, the complex potential dependent U-shape is found in both simulated and measured data. We note that this U-shape is observed not only in the acetate selectivity among C_2 products ($S_{\text{Ac}^-}^{\text{C}_2+}$) shown here, but can also be seen in acetate’s Faradaic efficiency

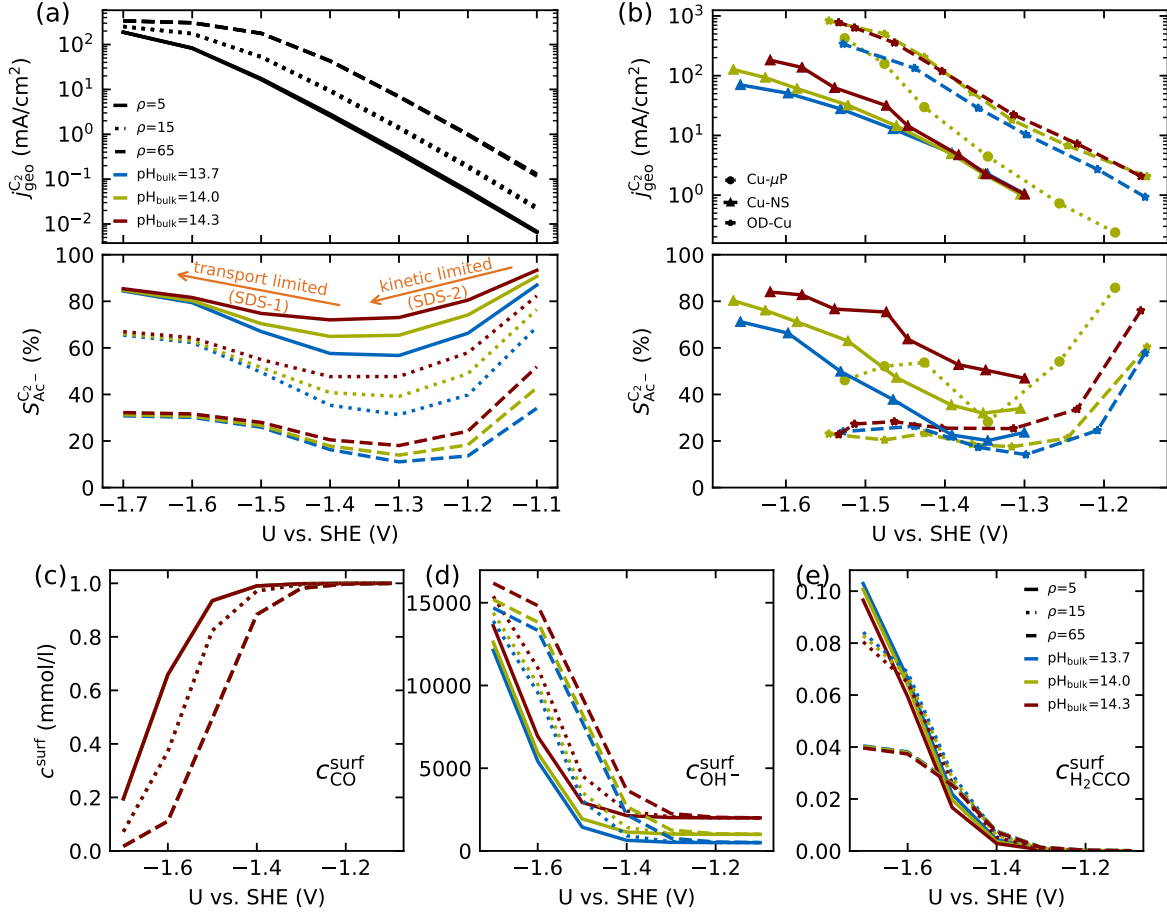


Figure 4: Geometric current densities ($j_{\text{geo}}^{\text{C}_2}$, top) and acetate selectivity among all C₂ products ($S_{\text{Ac}}^{\text{C}_2}$, bottom) against U_{SHE} as simulated by our transport coupled microkinetic model (a) and experimentally measured (b). Each line represents an individual data set of same reaction conditions. The different colors represent varying electrolyte pH and the solid, dotted, and dashed lines experiments and simulations with Cu-NS or $\rho = 5$, Cu- μ P or $\rho = 15$, and OD-Cu or $\rho = 65$, respectively. The experimental data is adapted from 4, 11. Note that the simulated $j_{\text{geo}}^{\text{C}_2}$ is invariant to pH as it follows the pH independent RDS of the C₂ products and competition to C₁ and HER or cation effects⁴¹ are not included in our model. The dominating selectivity mechanisms including kinetic (i) and transport (ii) competition are indicated (see text). (bottom) Surface concentrations of CO (c), OH⁻ (d), and H₂CCO (e) against potential for different electrolyte pH and roughness.

(see SI Fig. S1).

At higher overpotentials, there is a pH dependence of activities in the experimental data in Fig. 4b. We note that we did not include the competing pH dependent C_1 pathway or ion concentration effects^{1,41} in our simulations which could reproduce such an apparent pH dependence. Other/smaller quantitative deviation may originate in uncertainty of assumed flow-rates and the charge-neutral approximation or neglected size effects in our Nernst-Planck formulation in the transport model.

The critical variables that actually determine acetate selectivity are ρ and $c_{\text{OH}^-}^{\text{surf}}$. In general, acetate selectivity is optimized by (see Fig. S5):

- A lower ρ which favors transport of $\text{H}_2\text{CCO}(\text{aq})$ away from the surface due to a more favorable $A_{\text{geo}}/A_{\text{ECSA}}$ ratio.
- A higher $c_{\text{OH}^-}^{\text{surf}}$ which accelerates the solution reaction $\text{H}_2\text{CCO}(\text{aq})$ to Ac^-

These variables – depending on electrolysis conditions and catalyst morphology – originate in the influence of transport on SDS-1 (see Fig. 2). The following expression captures the importance of these two variables in the ratio of the interfacial flux of acetate (f_{Ac^-}) and other C_2 product:

$$R_{\text{Ac}^-}^{C_2} = \frac{f_{\text{Ac}^-}}{f_{\text{H}_2\text{CCO}}^{\text{ads}}} = \frac{c_{\text{H}_2\text{CCO}}^{\text{surf}} \cdot \sqrt{D_{\text{H}_2\text{CCO}} \cdot c_{\text{OH}^-}^{\text{surf}} \cdot k_{\text{sol}}}}{\rho \cdot c_{\text{H}_2\text{CCO}}^{\text{surf}} \cdot \theta^* \cdot k_{\text{H}_2\text{CCO}}^{\text{ads}}} = \frac{\sqrt{D_{\text{H}_2\text{CCO}} \cdot c_{\text{OH}^-}^{\text{surf}} \cdot k_{\text{sol}}}}{\rho \cdot \theta^* \cdot k_{\text{H}_2\text{CCO}}^{\text{ads}}} \quad (1)$$

where $c_{\text{H}_2\text{CCO}}^{\text{surf}}$ is the surface concentration and $D_{\text{H}_2\text{CCO}}$ the diffusion coefficient of ketene, k_{sol} the solution reaction constant, $k_{\text{H}_2\text{CCO}}^{\text{ads}}$ the adsorption constant of ketene, θ^* the amount of free sites on the catalyst surface, and the ratio $R_{\text{Ac}^-}^{C_2}$ relates to the acetate selectivity among C_2 products $S_{\text{Ac}^-}^{C_2} = f_{\text{Ac}^-} / (f_{\text{H}_2\text{CCO}}^{\text{ads}} + f_{\text{Ac}^-})$. Equ. 1 captures the aforementioned trends with respect to ρ and pH, and shows that other decisive factors determining acetate selectivity are the H_2CCO diffusion, the rate of the solution reaction, and the (re-)adsorption rate of H_2CCO . We derived the analytical expression in the numerator of Equ. 1 for a simplified

reaction-diffusion system of the solution reaction to acetate (see SI Sec. 7). Both f_{Ac^-} and f_{C_2} have a first order dependence on $c_{\text{H}_2\text{CCO}}^{\text{surf}}$. Therefore, acetate selectivity has no net dependence on the ketene surface concentration. With no dependence on the latter and no potential dependent barriers, the only potential dependence in SDS-1 results from the local pH ($c_{\text{OH}^-}^{\text{surf}}$). This constitutes the main potential dependence at high overpotentials (see Fig. 4), at low overpotentials SDS-2 is dominant. The square-root dependence of $c_{\text{OH}^-}^{\text{surf}}$ (see SI Sec. 7) scales weaker than the linear dependence of ρ which explains why an increase in ρ does not cancel with an increase in $c_{\text{OH}^-}^{\text{surf}}$ due to the accompanied change in local pH at high current densities.

Short diffusion lengths of ketene suggest that micro-, not macroscopic roughness determines acetate selectivity

We note that, due to the presence of the solution reaction between H_2CCO and OH^- , the diffusion length L_d for H_2CCO is extremely short. Fig. 5b shows that, under reasonable potentials and model parameters, all H_2CCO has reacted to acetate within 200 nm of the catalyst surface. This length scale is not only well within a size of a pore of a GDE electrode^{6,15,39} but on the same order of magnitude as the diameter of the catalyst particles d_P used for the experiments^{4,11} in Fig. 4b. As illustrated schematically in Fig. 5c, the small L_d means that the diffusion spheres around the nanoparticles do not overlap. Furthermore, the length scale of roughness features that define the competition between kinetics and mass transport in our selectivity mechanism, have length scales smaller than L_d . We therefore define ρ in our model as a *microscopic* roughness $A_{\text{real}}/A_{\text{smooth}}$, where A_{smooth} corresponds to the area of an ideal, smooth nanoparticle. This definition of the roughness fulfills its general definition $A_{\text{ECSA}}/A_{\text{geo}}$, but not *vice versa*. Therefore, changes in catalyst loading (which alter

$A_{\text{ECSA}}/A_{\text{geo}}$) do not alter ρ and should therefore lead to no changes in the acetate selectivity. This is true unless the diffusion spheres overlap significantly which would be the case for very small nanoparticles with diameters below 25-50 nm at a high loading (see Fig. 5d).

We evaluated this idea through measurements of CO reduction on micron sized Cu particles (Cu- μ P) at different loadings in 1M KOH in the same experimental setup as ref. 4, 11. Note that by changing only the loading of Cu particles, the morphology of the catalyst and its microscopic surface roughness ρ remain the same. With higher loadings, the geometric current densities of both total and CORR increase, but the current densities coincide after mass normalization (see Fig. S2). This alignment with normalization suggests that the higher current densities at higher loadings are due to the increased active area with the same intrinsic activity. As shown in Fig. 5a, also the same selectivity of acetate among the C_2 products within the range of 0.05 to 1.2 mg cm⁻² is found which appears to follow the same potential dependence and therefore mechanism as describe above (see Fig. 4a and b). The unchanged acetate selectivity confirms that it is not the loading-dependent macroscopic roughness but the morphology dependent microscopic roughness (ρ) that affects the selectivity towards the solution reaction. These findings of the loading experiments are consistent with the small diffusion lengths of the solution reaction. They highlight the corresponding importance of the local, microscopic variations in the structure of the Cu catalysts, as suggested by the model.

We emphasize that the relevance of the microscopic length scale here arises from the rapid solution reaction which leads to a very short diffusion length (compare Fig. 5). For intermediates that do not react in solution it has been shown in ORR (for H_2O_2) and methanol oxidation (for formaldehyde and formic acid) that the macroscopic roughness (hence the loading) also influences their degree of re-adsorption and further reduction.¹⁸ This difference is due to the larger diffusion lengths expected for pure diffusion processes as illustrated in Fig. 5c.

The different influence of the micro- and macroscopic roughness may also explain the

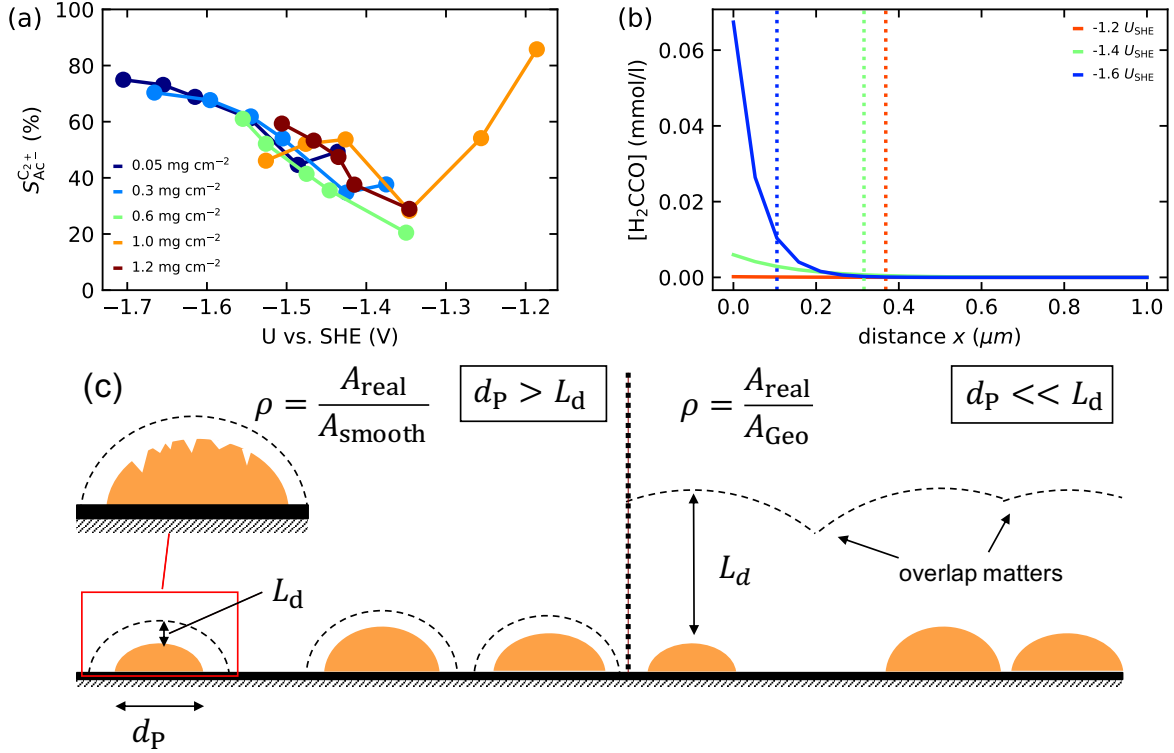


Figure 5: (a) Acetate selectivity among all C_2 products ($S_{AC^-}^{C_2+}$) against U_{SHE} for experiments with GDEs of different Cu- μ P loadings. Each line represents an individual data set of same reaction conditions. (b) Concentration profile of ketene given by our mass transport model within the electrode at different potentials vs. SHE. (c) Illustration of the effect of the diffusion length L_d in comparison to the particle diameter d_p , loading and the roughness ρ relevant to transport effects. At short L_d the overlap of diffusion spheres is negligible and only the local roughness matters (compared to a smooth particle surface). At long L_d diffusion spheres overlap and loading affects selectivity.

deviation of the relative $S_{\text{Ac}}^{\text{C}_2}$ between the experimental Cu-NS and Cu- μ P and the simulated $\rho = 5$ and 15 data in Fig. 4. The experimental roughness was determined at slightly different catalyst loadings^{4,11} which influences the macroscopic roughness but not the microscopic roughness ρ . This inconsistency justifies the deviation between experiment and simulation and demonstrates that a relative ρ can only be reliably determined at the same catalyst loading.

Why alternative pathways are unlikely

Since our mechanism in Fig. 2 is derived from DFT simulations, there may be inherent errors in the predicted energetics⁴² and barriers and therefore uncertainties in the resultant pathways. Supporting our proposed mechanism, we discuss here why previously proposed^{11–13} and other alternative pathways are unlikely, from a theoretical analysis of the experimentally observed pH and potential dependence in the activity.

Acetate selectivity cannot be determined by a CPET. The pH dependence of acetate in comparison to other C_2 products is only possible with OH^- as a reactant in contrast to a recent study¹² which proposed an early CPET reaction as the SDS towards acetate. On a potential vs. SHE scale, CPET reactions in alkaline conditions, where water is a proton donor, are either pH independent⁴³ (where the RDS is the first CPET) or show a decrease in activity as pH increases (where the RDS is the 2nd or later CPET)³² (also see SI Sec. 6). In contrast, as shown in Fig. 4, the activity for acetate increases with pH in relation to other C_2 products. Since the latter do not depend on pH on an SHE scale^{1,32,44} (or have even an apparent increasing activity with pH as visible in Fig. 4) it follows that the SDS of acetate must in turn have an intrinsic pH dependence (which is greater than the apparent C_2 one). This is only possible if OH^- is a reactant in the SDS, since the involvement of OH^- would lead to the necessary intrinsic pH dependence when involved in any reaction step prior to, coinciding with, or after the RDS.

Acetate does not have a RDS separate from other major C_2 products. Our assumption of a

shared RDS between acetate and other C_{2+} products is the most likely scenario and has also been assumed in previous work.^{11–13} As Fig. 1 shows, the total C_2 ’s, ethanol, ethylene, and acetate follow the same experimental trends: They share similar Tafel slopes (see 11 and Fig. 1) and a missing Nernstian pH dependence.³² Further, an otherwise separate RDS of acetate would need to be a potential dependent reaction with OH^- on the catalyst surface to yield the pH and potential dependence in acetate activity. Such a reaction step would, however, correspond to an oxidation reaction since OH^- would need to discharge.

The SDS for acetate does not involve OH^- in a surface reaction. Alternative to our suggested solution reaction, a hydrolysis on the catalyst surface has been suggested.^{11,13} This reaction would imply a nucleophilic attack of OH^- occurring on the negatively charged surface onto H_2CCO^* (or another early intermediate). Such a step appears highly improbable due to electrostatic repulsion, oxidative nature of the process and limited steric accessibility of the surface bound carbon atoms in those intermediates. Simulating this reaction for H_2CCO^* , we indeed find it associated with a high reaction barrier of $\Delta G^\ddagger = 0.8\text{ eV}$ and potential dependence (see SI Sec. 3.2) which is inconsistent with the experimental behavior.

The selectivity determining step(s) for acetate do not involve competing CPET vs. chemical reaction steps at high overpotentials. Refs 13 and 12 have, on the basis of reaction thermodynamics and barriers, suggested the selectivity towards acetate to be solely determined by the competition between a chemical surface reaction towards acetate vs. a CPET towards other C_2 products. However, this mechanism is unlikely since an increase in potential would mean an *exponential* increase in the rate of the CPET step towards other C_2 products, which would result in negligible amounts of acetate (compare potential dependence SDS-2). In contrast, SDS-1 in the present work, which determines the selectivity behaviour at high overpotentials, reflects a competition between H_2CCO re-adsorption towards C_2 products and a solution reaction towards acetate, and neither of these steps are CPET (as it proceeds SDS-2, it compensates its potential dependence). The corresponding coupled transport-kinetic model (Fig. 4) shows significant selectivities for both acetate and C_2 ’s over

a potential range consistent with experiments. The inconsistency of previously proposed SDS’s with the potential dependence in the selectivity of acetate vs. other C_2 ’s highlights the necessity of evaluating the rates of reaction in a microkinetic model to validate proposed mechanisms.

A Cannizzaro-type reaction is less likely than ketene hydrolysis in solution phase. The Cannizzaro reaction has been suggested as a possible source for acetate formation.^{34,35,45} Since this solution-based disproportionation reaction of acetaldehyde to acetate and ethanol is also OH^- catalyzed, it would yield the same trends with pH and roughness as ketene hydrolysis. It would, however, also yield a 50:50 ratio of ethanol and acetate which is experimentally never found. Even if a substantial part of the additional ethanol would be oxidized to acetate at the anode,²¹ a slight increased ethanol yield with pH and roughness should still be expected. Experimentally, the opposite trend is found,^{11,12} which renders this mechanism unlikely.

The ketene pathway is most likely the main C_2 pathway. We assume in our computational model that all C_2 products go through the ketene mechanism. This assumption is supported by acetate selectivities $> 80\%$ and direct FE competition between acetate and all other C_2 products in the experiments of Refs 4, 11 as shown in Fig. 4 and S3, respectively. Contrary to these observations, recent experiments at $< -1.9 V_{SHE}$ showed that acetate can be obtained as the sole liquid product, out-competing nearly all ethanol, while ethylene is less affected.¹² Our DFT simulations can also not provide a clear picture in that matter. An early bifurcation from the ketene pathway via the reduction of $HCCO^*$ to $HCCOH^*$ instead of H_2CCO (aq) at very high overpotentials may be likely, but within the typical DFT error very uncertain (see SI Sec. 3.1). While most available data suggests that the ketene pathway is the main C_{2+} pathway, we cannot exclude other pathways. However, the uncertainty about additional mechanisms does not affect the preceding arguments about selectivity since the contribution of any prior bifurcation must be small, given the overall high acetate yields.

Conclusion

In summary, we have presented a mechanism towards acetate in CO₂RR based on the solution reaction of ketene which elucidates the dependence of its selectivity on potential, pH and microscopic roughness. We gained this insight by an analysis of available GDE/flow cell and H-cell data, an experimental investigation of the effect of catalyst loading, and with the development of a multiscale model that predicts trends in selectivity vs. roughness, pH, and potential consistent with experiment. Our simulations show that the acetate selectivity is determined by the transport and subsequent solution reaction of ketene vs. its (re-)adsorption and further reduction at the catalyst surface.

We emphasize that we have not invoked any special active site(s) towards acetate in our model; the effect of nanostructuring is captured by a single roughness parameter and the effect of roughness arises from its effect on the interplay between transport and kinetics. Our examination of available ECSA-normalized data on nanostructured Cu suggests that active site(s) to be same across all types of Cu investigated thus far.

In general, our proposed mechanism and its implications are valid for both CORR and CO₂RR. However, the latter usually contains a reduced local pH due to the equilibrium of CO₂ with bicarbonate⁴ which gives rise to low acetate yields. An exception are highly alkaline electrolytes, i.e. 10M KOH (pH \approx 15).⁴⁶ Similarly, high yields of acetate at high overpotentials are less often seen in H-cell experiments, since high current densities are not achievable which would lead to the necessarily high local pH values (pH \geq 14-15, compare SI Fig. S10).

The proposed solution reaction of ketene is also in line with a recent study where amines are co-feed to CORR.¹³ A competing solution reaction of ketene with OH⁻ or amines explains the studys' selectivity trends with potential, pH, and amine identity.

Based on our insight, we propose the following strategies to maximize or minimize acetate yields: Generally, a high pH, a low catalyst roughness, and very high (≥ -1.2 V_{SHE}) or very low potentials (≤ -1.5 V_{SHE}) maximize the acetate yield. To obtain reasonable current

densities with high acetate selectivity a catalyst with a low to medium roughness $\rho \leq 10$ and high loading is required (a medium instead of a low roughness leads to increased current densities and stability⁹). The reaction should occur at low potentials and/or in very alkaline CORR conditions, similar to recent work.^{11,12} In contrast, a low acetate selectivity follows an operation of a very rough catalyst in neutral conditions using a buffer and intermediate potentials in the range of -1.6 to -1.3 V_{SHE}.

The presented mechanism rationalizes the trends in acetate selectivity based on the transport of stable intermediates/products. We note that a similar transport related process based on desorption vs. reduction (but no solution reaction) has been found for ORR and methanol oxidation¹⁸ and may also be relevant for other stable intermediates in CO₍₂₎RR like CO and acetaldehyde. This work highlights the importance of a rigorous evaluation of intrinsic catalyst activities and the potential impact of the interplay of reaction energetics, solution phase reactions, and mass transport in mechanistic studies of CO₍₂₎RR and beyond. From a simulation perspective, the combination of these effects on multiple length scales requires rigorous multiscale models and goes beyond usual approaches focusing only on the reaction energetics on the catalyst surface.

Methods

Loading experiments

The loading experiments were conducted using commercial 1 μm Cu particles (Alfa Aesar) as a cathode with IrO₂ (Alfa Aesar) as an anode. To prepare the catalyst ink, 25 mg of catalyst was dispersed in 3 ml of isopropanol and 20 μl of Nafion ionomer (10 wt% in H₂O) then the ink was drop-casted onto Sigracet 29 BC GDL (Fuel Cell Store). The loading varied from 0.05 to 1.2 mg cm⁻² for Cu (cathode) while the loading for IrO₂ kept at 0.5 mg cm⁻². The CO electrolysis was performed in a three-channel flow cell. The dimension of the channel was 2 cm \times 0.5 cm \times 0.15 cm with 1 cm² of the electrode area. The cathode and anode were

separated by an anion exchange membrane (FAA-3, Fumatech). The CO was fed into the cell at 15 sccm controlled using a mass flow controller. 1 M KOH solution (99.99%, Sigma-Aldrich) was used as both the catholyte and anolyte. The cathode potential was measured using an external Ag/AgCl reference electrode and converted to the standard hydrogen electrode (SHE) scale with 100% iR correction. During the electrolysis, the gas products were identified/quantified using a Multiple Gas Analyzer no. 5 gas chromatography equipped with a thermal conductivity detector and a flame ionization detector. The liquid products were collected from the outlet of the flow cell and quantified by ^1H NMR spectroscopy (Bruker AVIII 600 MHz NMR spectrometer) using dimethyl sulfoxide (Alfa Aesar) as an internal standard.

DFT calculations

DFT calculations were conducted using the BEEF-vdW⁴⁷ exchange-correlation functional. All thermodynamics were computed with GPAW^{48,49} where an electrochemical environment was mimicked using a hybrid explicit/implicit solvation scheme including a static water layer.³³ Our GPAW results compared well with results obtained in QuantumEspresso⁵⁰ in combination with the self-consistent continuum solvation (SCCS) model.⁵¹ Electrochemical reaction thermodynamics were referenced via the computational hydrogen electrode (CHE).⁵² We applied the corrections by Christensen *et al.* to mitigate systematic DFT errors.⁴² Free energies were obtained following the ideal gas law for gas phase species and the harmonic oscillator model for adsorbates, respectively. All possible surface adsorbates were thoroughly sampled for their most stable adsorption site on each Cu facet using the package CatKit.⁵³ From this sampling intermediates prior to HCCO^* were selected for each reduction stage according to their thermodynamic stability. The grand canonical CPET barriers were computed in alkaline conditions (H_2O as proton donor) using the SJM-model^{33,54} including an explicit water layer. We note that the calculations of electrochemical barriers still bear some uncertainties,^{55,56} so we cautiously take these results as tentative. However,

we note that the calculation of alkaline CPET barriers in this work was only possible due to the use of this grand canonical framework, due to spontaneous coadsorption of OH^- in conventional transition state searches. For handling of atomic structures, geometry optimizations, vibration calculations and nudged-elastic-band (NEB)⁵⁷ calculations, the Atomic Simulation Environment (ASE) package⁵⁸ was used. For further details of DFT calculations, slab models and convergence criteria see SI Sec. 2.

Coupled microkinetic and transport model

The microkinetic model was solved for its steady-state using an ODE solver available in the SciPy distribution.⁵⁹ Lateral interactions were ignored as they appear insensitive to the investigated mechanism, to ease the solution of the microkinetic model we adjusted the CO adsorption energy (see SI Sec. 5.5.3). The mass transport followed a hierarchical multiscale model where the transport within the GDE is solved via a 1-D model employing the electro-neutral Nernst-Planck equation^{37,60} and outside of the electrode described by effective mass transport relations.^{38–40} The transport of CO was assumed solely from the gaseous side and solved analytically with a short diffusion layer of 350 nm, necessary to achieve the high current densities (see Fig. 4). On the gaseous side the partial pressure of CO was assumed with 1 atm and its aqueous solubility by the Henry constant.⁶¹ The transport of OH^- and H_2CCO and their solution reaction was numerically solved for a diffusion length of 1 μm , within which the solution reaction is completed (see Fig. 5). Beyond the diffusion layer the electrode/electrolyte interface is assumed where the OH^- concentration is determined through a Sherwood relation describing the flow perpendicular to the catalyst surface.^{39,40} The microkinetic and transport models are iteratively solved for the catalyst surface concentrations. More details about the transport coupled microkinetic model can be found in the SI Sec. 5.

Code & Data availability

The code for the coupled microkinetic and transport model with all input data used in this work as well as the digitized data from Fig. 1 is available under the MIT License (<https://opensource.org/licenses/MIT>) and CC BY 4.0 (<https://creativecommons.org/licenses/by/4.0/>), respectively, in Zenodo (<https://doi.org/10.5281/zenodo.5013854>).

Acknowledgments

The research leading to these results has received funding from the European Union’s Horizon 2020 research and innovation programme under grant agreement No 851441, SELECTCO2. Financial support was provided by V- Sustain: The VILLUM Centre for the Science of Sustainable Fuels and Chemicals (#9455) from VILLUM FONDEN. The authors at the University of Delaware thank the National Science Foundation for financial support (Award No. CBET-1904966).

References

1. Nitopi, S.; Bertheussen, E.; Scott, S. B.; Liu, X.; Engstfeld, A. K.; Horch, S.; Seger, B.; Stephens, I. E.; Chan, K.; Hahn, C. *et al.* Progress and perspectives of electrochemical CO₂ reduction on copper in aqueous electrolyte. *Chem. Rev.* **2019**, *119*, 7610–7672.
2. Jouny, M.; Luc, W.; Jiao, F. General techno-economic analysis of CO₂ electrolysis systems. *Ind. Eng. Chem. Res.* **2018**, *57*, 2165–2177.
3. De Luna, P.; Hahn, C.; Higgins, D.; Jaffer, S. A.; Jaramillo, T. F.; Sargent, E. H. What would it take for renewably powered electrosynthesis to displace petrochemical processes? *Science* **2019**, *364*.

4. Jouny, M.; Luc, W.; Jiao, F. High-rate electroreduction of carbon monoxide to multi-carbon products. *Nat. Catal.* **2018**, *1*, 748–755.
5. Dinh, C.-T.; Burdyny, T.; Kibria, M. G.; Seifitokaldani, A.; Gabardo, C. M.; De Arquer, F. P. G.; Kiani, A.; Edwards, J. P.; De Luna, P.; Bushuyev, O. S. *et al.* CO₂ electroreduction to ethylene via hydroxide-mediated copper catalysis at an abrupt interface. *Science* **2018**, *360*, 783–787.
6. Burdyny, T.; Smith, W. A. CO₂ reduction on gas-diffusion electrodes and why catalytic performance must be assessed at commercially-relevant conditions. *Energy Environ. Sci.* **2019**, *12*, 1442–1453.
7. Li, C. W.; Kanan, M. W. CO₂ reduction at low overpotential on Cu electrodes resulting from the reduction of thick Cu₂O films. *J. Am. Chem. Soc.* **2012**, *134*, 7231–7234.
8. Li, C. W.; Ciston, J.; Kanan, M. W. Electroreduction of carbon monoxide to liquid fuel on oxide-derived nanocrystalline copper. *Nature* **2014**, *508*, 504–507.
9. Kas, R.; Yang, K.; Bohra, D.; Kortlever, R.; Burdyny, T.; Smith, W. A. Electrochemical CO₂ reduction on nanostructured metal electrodes: fact or defect? *Chem. Sci.* **2020**, *11*, 1738–1749.
10. Resasco, J.; Bell, A. T. Electrocatalytic CO₂ reduction to fuels: progress and opportunities. *Trends Chem.* **2020**,
11. Luc, W.; Fu, X.; Shi, J.; Lv, J.-J.; Jouny, M.; Ko, B. H.; Xu, Y.; Tu, Q.; Hu, X.; Wu, J. *et al.* Two-dimensional copper nanosheets for electrochemical reduction of carbon monoxide to acetate. *Nat. Catal.* **2019**, *2*, 423–430.
12. Zhu, P.; Xia, C.; Liu, C.-Y.; Jiang, K.; Gao, G.; Zhang, X.; Xia, Y.; Lei, Y.; Alsharreef, H. N.; Senftle, T. P. *et al.* Direct and continuous generation of pure acetic acid

- solutions via electrocatalytic carbon monoxide reduction. *Proc. Natl. Acad. Sci. U.S.A.* **2020**, *118*.
13. Jouny, M.; Lv, J.-J.; Cheng, T.; Ko, B. H.; Zhu, J.-J.; Goddard, W. A.; Jiao, F. Formation of carbon–nitrogen bonds in carbon monoxide electrolysis. *Nat. Chem.* **2019**, *11*, 846–851.
 14. Hall, A. S.; Yoon, Y.; Wuttig, A.; Surendranath, Y. Mesostructure-induced selectivity in CO₂ reduction catalysis. *J. Am. Chem. Soc.* **2015**, *137*, 14834–14837.
 15. Suter, S.; Haussener, S. Optimizing mesostructured silver catalysts for selective carbon dioxide conversion into fuels. *Energy Environ. Sci.* **2019**, *12*, 1668–1678.
 16. Raciti, D.; Mao, M.; Wang, C. Mass transport modelling for the electroreduction of CO₂ on Cu nanowires. *Nanotechnology* **2017**, *29*, 044001.
 17. Bohra, D.; Chaudhry, J. H.; Burdyny, T.; Pidko, E. A.; Smith, W. A. Modeling the electrical double layer to understand the reaction environment in a CO₂ electrocatalytic system. *Energy Environ. Sci.* **2019**, *12*, 3380–3389.
 18. Seidel, Y.; Schneider, A.; Jusys, Z.; Wickman, B.; Kasemo, B.; Behm, R. Mesoscopic mass transport effects in electrocatalytic processes. *Faraday Discuss.* **2009**, *140*, 167–184.
 19. Nørskov, J. K.; Studt, F.; Abild-Pedersen, F.; Bligaard, T. *Fundamental Concepts in Heterogeneous Catalysis*; John Wiley & Sons, Inc., 2014.
 20. Clark, E. L.; Resasco, J.; Landers, A.; Lin, J.; Chung, L.-T.; Walton, A.; Hahn, C.; Jaramillo, T. F.; Bell, A. T. Standards and protocols for data acquisition and reporting for studies of the electrochemical reduction of carbon dioxide. *ACS Catal.* **2018**, *8*, 6560–6570.

21. Ripatti, D. S.; Veltman, T. R.; Kanan, M. W. Carbon monoxide gas diffusion electrolysis that produces concentrated C₂ products with high single-pass conversion. *Joule* **2019**, *3*, 240–256.
22. Zhang, J.; Luo, W.; Züttel, A. Self-supported copper-based gas diffusion electrodes for CO₂ electrochemical reduction. *J. Mater. Chem. A* **2019**, *7*, 26285–26292.
23. Ma, M.; Clark, E. L.; Therkildsen, K. T.; Dalsgaard, S.; Chorkendorff, I.; Seger, B. Insights into the carbon balance for CO₂ electroreduction on Cu using gas diffusion electrode reactor designs. *Energy Environ. Sci.* **2020**, *13*, 977–985.
24. De Gregorio, G. L.; Burdyny, T.; Loiudice, A.; Iyengar, P.; Smith, W. A.; Buonsanti, R. Facet-dependent selectivity of Cu catalysts in electrochemical CO₂ reduction at commercially viable current densities. *ACS Catal.* **2020**, *10*, 4854–4862.
25. Wang, X.; Wang, Z.; de Arquer, F. P. G.; Dinh, C.-T.; Ozden, A.; Li, Y. C.; Nam, D.-H.; Li, J.; Liu, Y.-S.; Wicks, J. *et al.* Efficient electrically powered CO₂-to-ethanol via suppression of deoxygenation. *Nat. Energy* **2020**, *5*, 478–486.
26. (a) Bertheussen, E.; Verdaguer-Casadevall, A.; Ravasio, D.; Montoya, J. H.; Trimarco, D. B.; Roy, C.; Meier, S.; Wendland, J.; Nørskov, J. K.; Stephens, I. E. *et al.* Acetaldehyde as an intermediate in the electroreduction of carbon monoxide to ethanol on oxide-derived copper. *Angew. Chem. Int. Ed.* **2016**, *128*, 1472–1476; (b) Bertheussen, E.; Hogg, T. V.; Abghoui, Y.; Engstfeld, A. K.; Chorkendorff, I.; Stephens, I. E. Electroreduction of CO on polycrystalline copper at low overpotentials. *ACS Energy Lett.* **2018**, *3*, 634–640; (c) Wang, L.; Nitopi, S. A.; Bertheussen, E.; Orazov, M.; Morales-Guio, C. G.; Liu, X.; Higgins, D. C.; Chan, K.; Nørskov, J. K.; Hahn, C. *et al.* Electrochemical carbon monoxide reduction on polycrystalline copper: Effects of potential, pressure, and pH on selectivity toward multicarbon and oxygenated products. *ACS Catal.* **2018**, *8*, 7445–7454; (d) Wang, L.; Nitopi, S.; Wong, A. B.; Snider, J. L.; Nielander, A. C.;

- Morales-Guio, C. G.; Orazov, M.; Higgins, D. C.; Hahn, C.; Jaramillo, T. F. Electrochemically converting carbon monoxide to liquid fuels by directing selectivity with electrode surface area. *Nat. Catal.* **2019**, *2*, 702–708; (e) Raciti, D.; Cao, L.; Livi, K. J.; Rottmann, P. F.; Tang, X.; Li, C.; Hicks, Z.; Bowen, K. H.; Hemker, K. J.; Mueller, T. *et al.* Low-overpotential electroreduction of carbon monoxide using copper nanowires. *ACS Catal.* **2017**, *7*, 4467–4472.
27. Kuhl, K. P.; Cave, E. R.; Abram, D. N.; Jaramillo, T. F. New insights into the electrochemical reduction of carbon dioxide on metallic copper surfaces. *Energy Environ. Sci.* **2012**, *5*, 7050–7059.
 28. Huang, Y.; Handoko, A. D.; Hirunsit, P.; Yeo, B. S. Electrochemical reduction of CO₂ using copper single-crystal surfaces: effects of CO* coverage on the selective formation of ethylene. *ACS Catal.* **2017**, *7*, 1749–1756.
 29. Andraos, J.; Kresge, A. J. Correlation of rates of uncatalyzed and hydroxide-ion catalyzed ketene hydration. A mechanistic application and solvent isotope effects on the uncatalyzed reaction. *Can. J. Chem.* **2000**, *78*, 508–515.
 30. Schouten, K. J. P.; Pérez Gallent, E.; Koper, M. T. Structure sensitivity of the electrochemical reduction of carbon monoxide on copper single crystals. *ACS Catal.* **2013**, *3*, 1292–1295.
 31. Montoya, J. H.; Shi, C.; Chan, K.; Nørskov, J. K. Theoretical insights into a CO dimerization mechanism in CO₂ electroreduction. *J. Phys. Chem. Lett.* **2015**, *6*, 2032–2037.
 32. Liu, X.; Schlexer, P.; Xiao, J.; Ji, Y.; Wang, L.; Sandberg, R. B.; Tang, M.; Brown, K. S.; Peng, H.; Ringe, S. *et al.* pH effects on the electrochemical reduction of CO₂ towards C₂ products on stepped copper. *Nat. Commun.* **2019**, *10*.
 33. Kastlunger, G.; Lindgren, P.; Peterson, A. A. Controlled-potential simulation of elemen-

- tary electrochemical reactions: Proton discharge on metal surfaces. *J. Phys. Chem. C* **2018**, *122*, 12771–12781.
34. Lum, Y.; Cheng, T.; Goddard III, W. A.; Ager, J. W. Electrochemical CO reduction builds solvent water into oxygenate products. *J. Am. Chem. Soc.* **2018**, *140*, 9337–9340.
 35. Clark, E. L.; Wong, J.; Garza, A. J.; Lin, Z.; Head-Gordon, M.; Bell, A. T. Explaining the incorporation of oxygen derived from solvent water into the oxygenated products of CO reduction over Cu. *J. Am. Chem. Soc.* **2019**, *141*, 4191–4193.
 36. Hasa, B.; Jouny, M.; Ko, B. H.; Xu, B.; Jiao, F. Flow Electrolyzer Mass Spectrometry with a Gas-Diffusion Electrode Design. *Angew. Chem. Int. Ed.* **2020**,
 37. Subramaniam, A.; Chen, J.; Jang, T.; Geise, N. R.; Kasse, R. M.; Toney, M. F.; Subramanian, V. R. Analysis and Simulation of One-Dimensional Transport Models for Lithium Symmetric Cells. *J. Electrochem. Soc.* **2019**, *166*, A3806.
 38. Bohra, D.; Chaudhry, J.; Burdyny, T.; Pidko, E.; Smith, W. Mass Transport in Catalytic Pores of GDE-Based CO₂ Electroreduction Systems. **2020**,
 39. Modestino, M. A.; Hashemi, S. M. H.; Haussener, S. Mass transport aspects of electrochemical solar-hydrogen generation. *Energy Environ. Sci.* **2016**, *9*, 1533–1551.
 40. Cussler, E. L.; Cussler, E. L. *Diffusion: mass transfer in fluid systems*; Cambridge university press, 2009.
 41. Resasco, J.; Chen, L. D.; Clark, E.; Tsai, C.; Hahn, C.; Jaramillo, T. F.; Chan, K.; Bell, A. T. Promoter effects of alkali metal cations on the electrochemical reduction of carbon dioxide. *J. Am. Chem. Soc.* **2017**, *139*, 11277–11287.
 42. Christensen, R.; Hansen, H. A.; Vegge, T. Identifying systematic DFT errors in catalytic reactions. *Catal. Sci. Technol.* **2015**, *5*, 4946–4949.

43. Strmcnik, D.; Uchimura, M.; Wang, C.; Subbaraman, R.; Danilovic, N.; Van Der Vliet, D.; Paulikas, A. P.; Stamenkovic, V. R.; Markovic, N. M. Improving the hydrogen oxidation reaction rate by promotion of hydroxyl adsorption. *Nat. Chem.* **2013**, *5*, 300.
44. Hori, Y. i. *Modern aspects of electrochemistry*; Springer, 2008; pp 89–189.
45. Birdja, Y. Y.; Koper, M. T. The importance of cannizzaro-type reactions during electrocatalytic reduction of carbon dioxide. *J. Am. Chem. Soc.* **2017**, *139*, 2030–2034.
46. Wang, Y.; Shen, H.; Livi, K. J.; Raciti, D.; Zong, H.; Gregg, J.; Onadeko, M.; Wan, Y.; Watson, A.; Wang, C. Copper nanocubes for CO₂ reduction in gas diffusion electrodes. *Nano Lett.* **2019**, *19*, 8461–8468.
47. Wellendorff, J.; Lundgaard, K. T.; Møgelhøj, A.; Petzold, V.; Landis, D. D.; Nørskov, J. K.; Bligaard, T.; Jacobsen, K. W. Density functionals for surface science: Exchange-correlation model development with Bayesian error estimation. *Phys. Rev. B* **2012**, *85*, 235149.
48. Mortensen, J. J.; Hansen, L. B.; Jacobsen, K. W. Real-space grid implementation of the projector augmented wave method. *Phys. Rev. B* **2005**, *71*, 035109.
49. Enkovaara, J.; Rostgaard, C.; Mortensen, J. J.; Chen, J.; Dulak, M.; Ferrighi, L.; Gavnholt, J.; Glinsvad, C.; Haikola, V.; Hansen, H. A. *et al.* Electronic structure calculations with GPAW: a real-space implementation of the projector augmented-wave method. *J. Phys.: Condens. Matter* **2010**, *22*, 253202.
50. Giannozzi, P.; Baroni, S.; Bonini, N.; Calandra, M.; Car, R.; Cavazzoni, C.; Ceresoli, D.; Chiarotti, G. L.; Cococcioni, M.; Dabo, I. *et al.* QUANTUM ESPRESSO: a modular and open-source software project for quantum simulations of materials. *J. Phys. Condens. Matter* **2009**, *21*, 395502.

51. Andreussi, O.; Dabo, I.; Marzari, N. Revised self-consistent continuum solvation in electronic-structure calculations. *J. Chem. Phys.* **2012**, *136*.
52. Nørskov, J.; Rossmeisl, J.; Logadottir, A.; Lindqvist, L.; Kitchin, J.; Bligaard, T.; Jónsson, H. Origin of the Overpotential for Oxygen Reduction at a Fuel-Cell Cathode. *J. Phys. Chem. B* **2004**, *108*, 17886–17892.
53. Boes, J. R.; Mamun, O.; Winther, K.; Bligaard, T. Graph Theory Approach to High-Throughput Surface Adsorption Structure Generation. *J. Phys. Chem. A* **2019**, *123*, 2281–2285.
54. Lindgren, P.; Kastlunger, G.; Peterson, A. A. A Challenge to the G₀ Interpretation of Hydrogen Evolution. *ACS Catal.* **2019**, *10*, 121–128.
55. Gauthier, J. A.; Ringe, S.; Dickens, C. F.; Garza, A. J.; Bell, A. T.; Head-Gordon, M.; Nørskov, J. K.; Chan, K. Challenges in modeling electrochemical reaction energetics with polarizable continuum models. *ACS Catal.* **2018**, *9*, 920–931.
56. Gauthier, J. A.; Dickens, C. F.; Heenen, H. H.; Vijay, S.; Ringe, S.; Chan, K. Unified approach to implicit and explicit solvent simulations of electrochemical reaction energetics. *Journal of chemical theory and computation* **2019**, *15*, 6895–6906.
57. Lindgren, P.; Kastlunger, G.; Peterson, A. A. Scaled and Dynamic Optimizations of Nudged Elastic Bands. *Journal of chemical theory and computation* **2019**, *15*, 5787–5793.
58. Larsen, A. H.; Mortensen, J. J.; Blomqvist, J.; Castelli, I. E.; Christensen, R.; Dułak, M.; Friis, J.; Groves, M. N.; Hammer, B.; Hargus, C. *et al.* The atomic simulation environment—a Python library for working with atoms. *J. Phys. Condens. Matter* **2017**, *29*, 273002.

59. Virtanen, P.; Gommers, R.; Oliphant, T. E.; Haberland, M.; Reddy, T.; Cournapeau, D.; Burovski, E.; Peterson, P.; Weckesser, W.; Bright, J. *et al.* SciPy 1.0: fundamental algorithms for scientific computing in Python. *Nature methods* **2020**, *17*, 261–272.
60. Heenen, H. H.; Voss, J.; Scheurer, C.; Reuter, K.; Luntz, A. C. Multi-ion Conduction in Li3OCl Glass Electrolytes. *Journal Phys. Chem. Lett.* **2019**, *10*, 2264–2269.
61. Sander, R. Compilation of Henry’s law constants (version 4.0) for water as solvent. *Atmos. Chem. Phys* **2015**, *15*, 4399–4981.